4.2.7 Crack with $K_I = 0.289$ MPa$\sqrt{\text{m}}$ and $K_{II} = -2.9$ kPa$\sqrt{\text{m}}$

For this larger wedge displacement case in specimen HomC2, the experimental stress intensity factors are $K_I = 0.289$ MPa$\sqrt{\text{m}}$ and $K_{II} = -2.9$ kPa$\sqrt{\text{m}}$ with a mode-mixity ratio $\mu_{SIF} = -0.010$; thus this example has a similar moderate-level K_I as the $K_I = 0.259$ MPa$\sqrt{\text{m}}$ case for specimen HomC1, but with smaller magnitude, negative mode-mixity. The experimental parameters are the same for this load case as in the previous case.

Figures 4.57–4.59 present the photoelasticity and the vertical and horizontal shear CGS images. Since this specimen is thicker than HomC1, the fringes are closer in density to the $K_I = 0.514$ MPa$\sqrt{\text{m}}$ case than the $K_I = 0.259$ MPa$\sqrt{\text{m}}$ case. The small blur due to notch tip on the surface is still present in the images, but again do not appear to distort the field, and therefore a mask is sufficient to remove its influence. The weak Fizeau interference patterns in the photoelastic images are minimized used the Wiener filter with window size of $[25 \times 25]$ pixels before processing the data. Table 4.4 reports the RMSD values, data ranges, and NRMSD values for this $K_I = 0.289$ MPa$\sqrt{\text{m}}$ case. The NRMSD values are good for all of the fields ranging from 0.0019 to 0.063, with the highest value for σ_{xx}, which is still quite acceptable.

The isoclinic angle in Figure 4.60(a) for the $K_I = 0.289$ MPa$\sqrt{\text{m}}$ has the same form as the other cases, with (i) the radial symmetry about the crack tip, (ii) the NRMSD of 0.033, (iii) higher local errors where the wrapped α was manually corrected near the crack tip, (iv) the error of smoothing the data through 0 around $\theta = 0$, and (v) otherwise generally good comparison with theory. The theoretical isoclinic angle in this case slightly differs from those of the other cases near $\theta = 0$ due to the negative mode-mixity, as seen in Figure 4.60(c). The experimental and theoretical $\sigma_1 - \sigma_2$ fields in Figures 4.60(d) and 4.60(e) have generally good agreement with NRMSD of 0.048, except the stress concentrations at the crack tip are not as large in the experimental field, and the experimental stresses do not go towards zero near $\theta = 0$ as in the theoretical field.

The experimental and theoretical derivatives of $\sigma_1 + \sigma_2$ in Figure 4.61 compare very well globally. The experimental x derivative of $\sigma_1 + \sigma_2$ has the correct shape and stress concentration for the range of -20 MPa/mm to 20 MPa/mm, leading to an NRMSD of only 0.021, but does not quite obtain

Quantity	Units	RMSD (in Units)	Data Range (in Units)	NRMSD (No Units)
α	rad.	0.22	6.71	0.033
$\partial(\sigma_1 + \sigma_2)/\partial x$ from $\lambda/4$ plate method	MPa/mm	1.04	48.6	0.021
$\partial(\sigma_1 + \sigma_2)/\partial y$ from $\lambda/4$ plate method	MPa/mm	0.89	47.5	0.019
$\sigma_1 + \sigma_2$	MPa	0.71	12.5	0.056
$\sigma_1 - \sigma_2$	MPa	0.32	6.67	0.048
σ_1	MPa	0.41	9.05	0.046
σ_2	MPa	0.33	5.86	0.055
σ_{xx}	MPa	0.41	6.49	0.063
σ_{yy}	MPa	0.40	9.27	0.043
σ_{xy}	MPa	0.25	6.14	0.040
σ_{rr}	MPa	0.46	7.74	0.059
$\sigma_{\theta\theta}$	MPa	0.40	7.70	0.052
$\sigma_{r\theta}$	MPa	0.17	6.25	0.026

Table 4.4: Error analysis for various experimental fields for specimen HomC2 for $K_I = 0.289$ MPa$\sqrt{\text{m}}$ and $K_{II} = -2.9$ kPa$\sqrt{\text{m}}$

the localized higher stress concentration just behind the crack tip. The experimental y derivative of $\sigma_1 + \sigma_2$ does a good job of reaching close to the stress concentration at the sides of the crack tip, allowing for a good NRMSD of 0.019, though the derivative is a little small behind the crack tip. These smaller experimental derivatives behind the crack tip lead to an experimental $\sigma_1 + \sigma_2$ in Figure 4.61(e) that does not decrease enough towards zero along the crack as compared to the theoretical field in Figure 4.61(f). Elsewhere in the field, $\sigma_1 + \sigma_2$ matches theory well with a good stress concentration level at the crack tip. These experimental derivative fields appear to compare well because the CGS phase inherently better approximates the theoretical derivatives due to the smaller mode-mixity $\mu_{SIF} = -0.010$, evident in the lower ϵ error globally for the CGS fields in Figure 4.62. The errors in both shearing directions, but particularly in the vertical shearing direction, are markedly lower than for the highest mode-mixity case $\mu_{SIF} = 0.020$ that has a similar $K_I = 0.259$ MPa$\sqrt{\text{m}}$, implying that for modest mode-mixity cases employing CGS, the shearing direction related to the y derivative will most likely better represent a derivative than the other shearing direction. This observation is restricted to these low mode-mixity cases because this may not be true for larger mode-mixity, as seen in a mixed-mode fracture study by Mason et al. (1992) that demonstrated reasonable K_{II}/K_I calculation agreement with theory and finite elements.

The experimental and theoretical principal stresses in Figure 4.63 compare well in front of and close to the crack, but the experimental σ_2 is too large for $(-x, -y)$ data points due to the errors in $\sigma_1 + \sigma_2$ in that region, leading to the largest NRMSD for this case at 0.056. The Cartesian stresses in Figure 4.64 all exhibit the correct behavior and stress levels globally. The higher stress levels in the fish-shaped σ_{xx} extends further from the crack than predicted. The manually corrected regions near the crack tip in α appear to spread the side lobes located along the y axis in σ_{xy}, and the stresses seem higher in magnitude in the $+x$ region. The σ_{yy} field agrees well visually except for $(-x, -y)$ data points along the crack. The polar stresses in Figure 4.65 have similar NRMSD values as the Cartesian stresses, but appear to have more local errors. These visual differences are due to the manually corrected regions in α that slightly distort the radial symmetry of the theoretical α. Regardless of local errors, the experimental and theoretical polar stresses match well globally.

The σ_{yy} versus r line plots for $\theta = 0$ in Figure 4.66 indicate reasonable agreement in behavior with theory for $r < 1.5$ mm. The $1/\sqrt{r}$ behavior is excellent for $r < 1.5$ mm, but the slope of $\log \sigma_{yy}$ versus $\log r$ slightly increases for $r > 1.5$ mm. This is most likely due to experimental error since this is the opposite behavior from the smaller load case for the same specimen, but may be due to the finite size of the specimen; far from the crack, the stress field is not K-dominant due to boundary effects of a finite size specimen. The loss of K dominance far from the crack is usually indicated by a decrease (in magnitude) in the slope of the $\log \sigma_{yy}$ versus $\log r$ plot for $\theta = 0$, which is not the case here; thus, the errors in $\sigma_1 - \sigma_2$ and α are the likely error sources for σ_{yy}, since $\sigma_1 - \sigma_2$ is larger than predicted here. Given the reasonable agreement with $1/\sqrt{r}$ behavior of this case, the stress fields are likely in a K-dominant region of the crack. This case demonstrates the experimental method to determine full-field stresses for a moderate K_I with low mode-mixity. The same error sources appear in this case as with others, but these are well-characterized and possibly can be minimized with some improvements. This case does not appear to show any new errors, but does add to the range of capability of this experimental method.

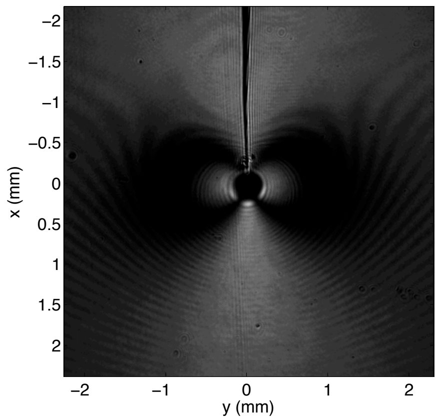

(a) $I_1 = I_o(1 + \cos(\delta))$

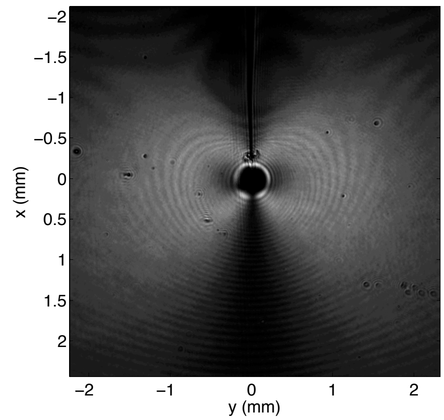

(b) $I_2 = I_o(1 - \cos(\delta))$

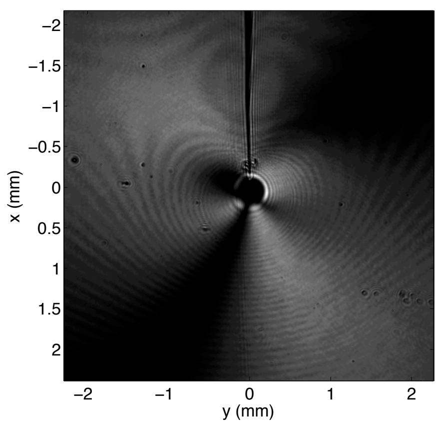

(c) $I_3 = I_o(1 - \sin(\delta)\sin(2\alpha))$

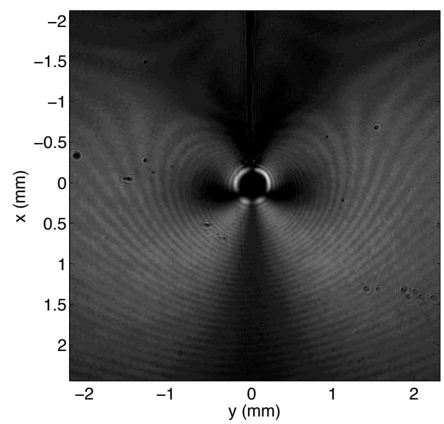

(d) $I_4 = I_o(1 + \sin(\delta)\cos(2\alpha))$

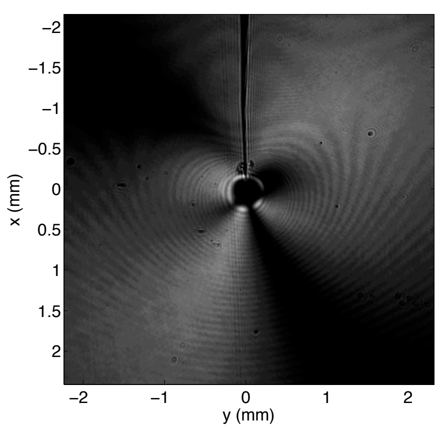

(e) $I_5 = I_o(1 + \sin(\delta)\sin(2\alpha))$

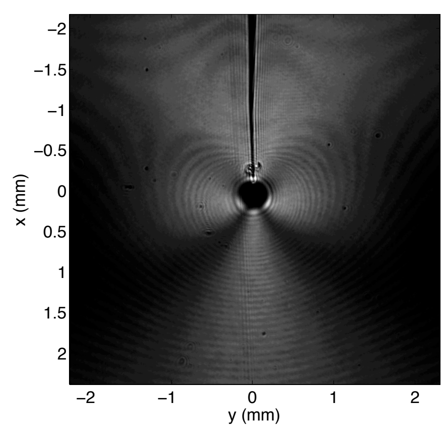

(f) $I_6 = I_o(1 - \sin(\delta)\cos(2\alpha))$

Figure 4.57: Experimental mages from six-step phase-shifting photoelasticity for specimen HomC2 for $K_I = 0.289$ MPa$\sqrt{\text{m}}$ and $K_{II} = -2.9$ kPa$\sqrt{\text{m}}$. Caustic shadows obscure the data at the crack tip due to the stress concentration, and the weak high density fringes overlaying the photoelastic fringes are due to the interference of the reflections from the front and back faces of the specimen

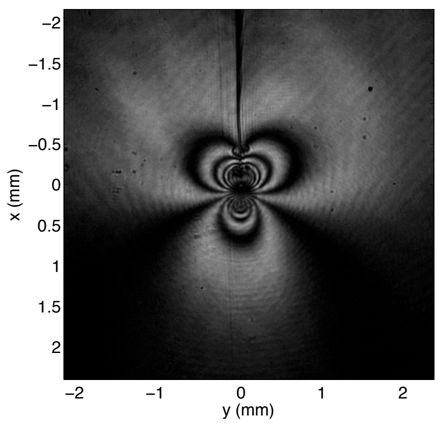

(a) I_1^{circ}

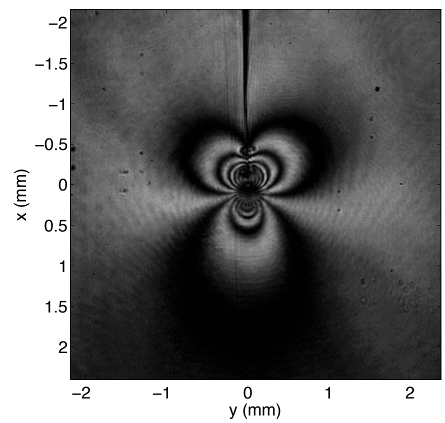

(b) I_2^{circ}

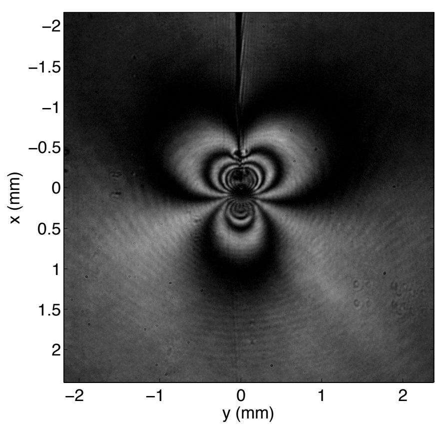

(c) I_3^{circ}

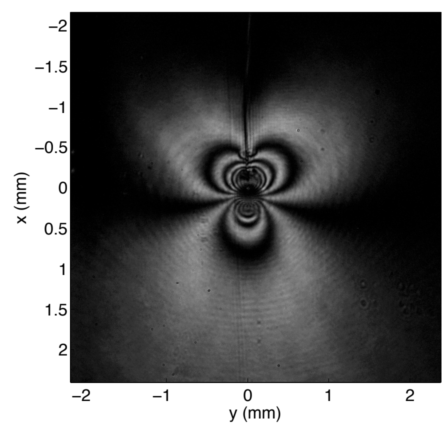

(d) I_4^{circ}

Figure 4.58: Experimental phase-shifted images from vertical shearing CGS using the $\lambda/4$ polarization method for specimen HomC2 for $K_I = 0.289$ MPa$\sqrt{\text{m}}$ and $K_{II} = -2.9$ kPa$\sqrt{\text{m}}$

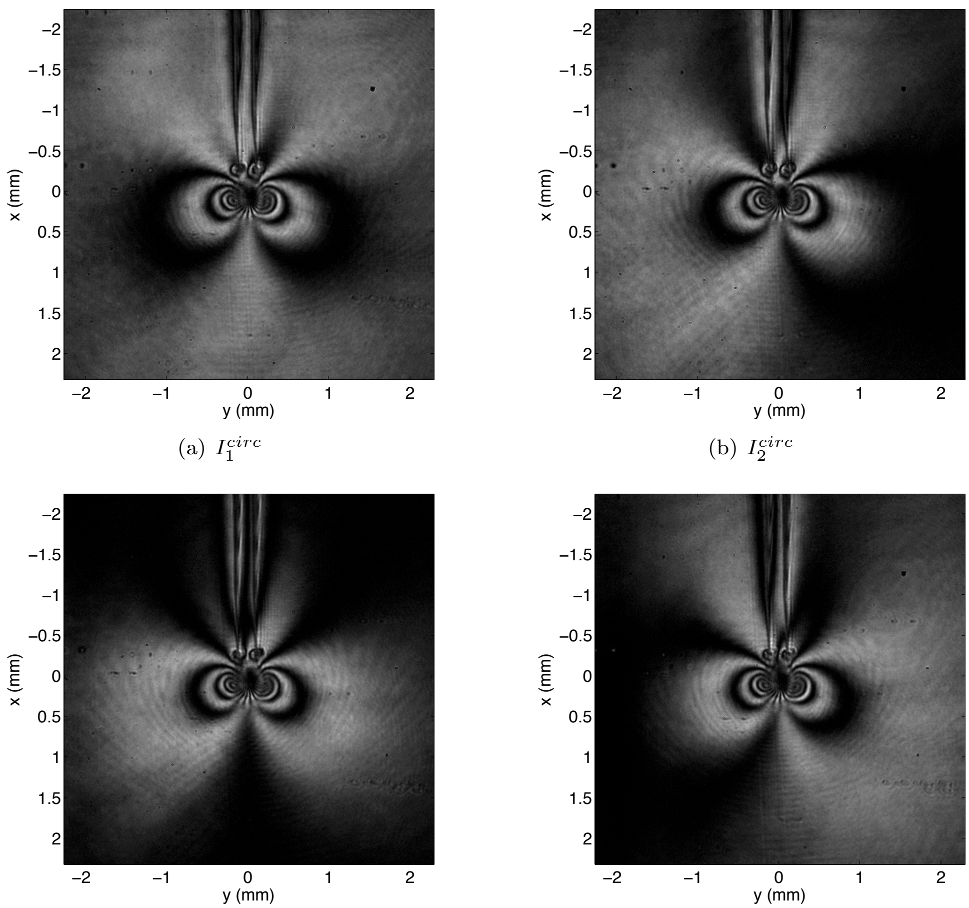

(a) I_1^{circc} (b) I_2^{circ}

(c) I_3^{circ} (d) I_4^{circ}

Figure 4.59: Experimental phase-shifted images from horizontal shearing CGS using the $\lambda/4$ polarization method for specimen HomC2 for $K_I = 0.289$ MPa$\sqrt{\text{m}}$ and $K_{II} = -2.9$ kPa$\sqrt{\text{m}}$

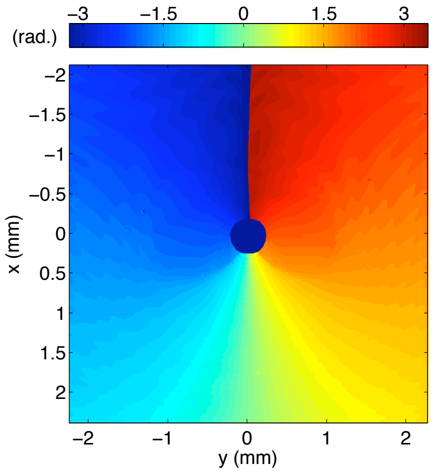

(a) Experimental unwrapped α

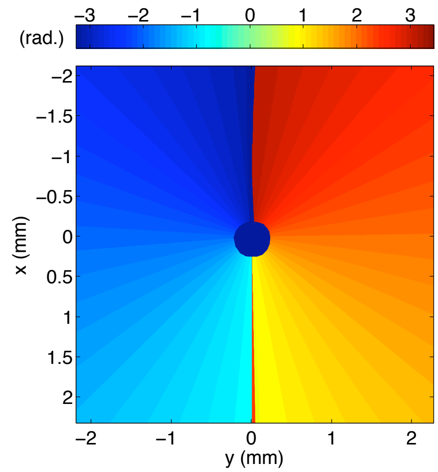

(b) Theoretical unwrapped α

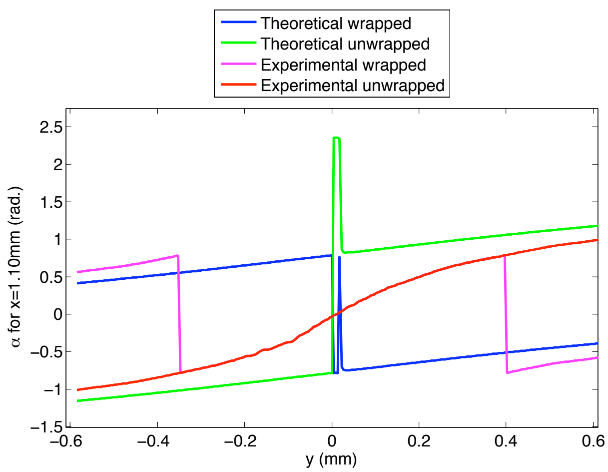

(c) Experimental and theoretical wrapped and unwrapped α

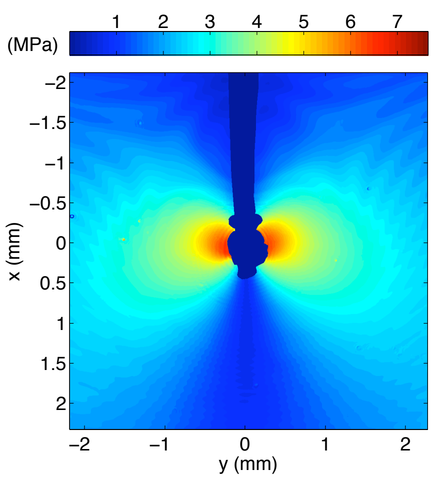

(d) Experimental $\sigma_1 - \sigma_2$

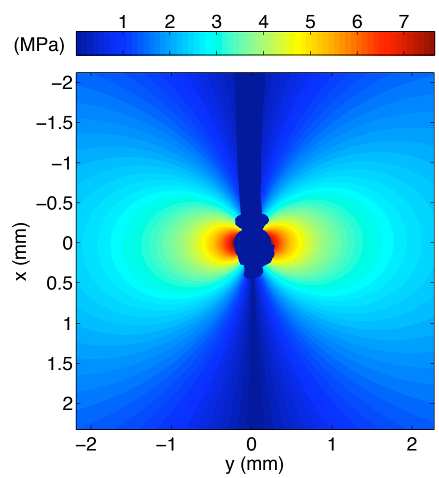

(e) Theoretical $\sigma_1 - \sigma_2$

Figure 4.60: Experimental and theoretical unwrapped isoclinic angle with crack region masked in blue and comparison of experimental and theoretical wrapped and unwrapped α for $x = 1.10$

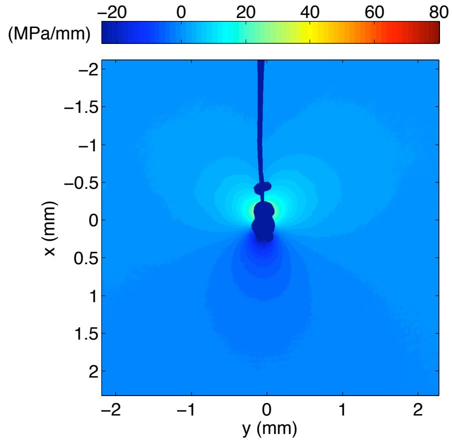

(a) Experimental $\frac{\partial(\sigma_1+\sigma_2)}{\partial x}$

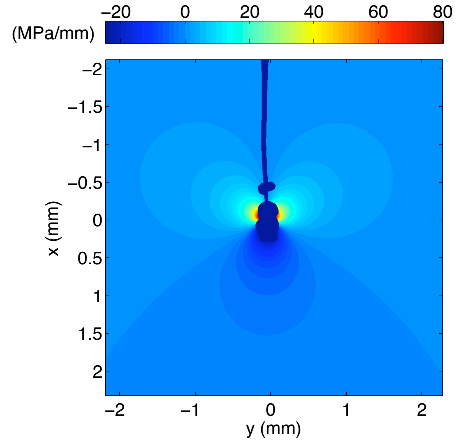

(b) Theoretical $\frac{\partial(\sigma_1+\sigma_2)}{\partial x}$

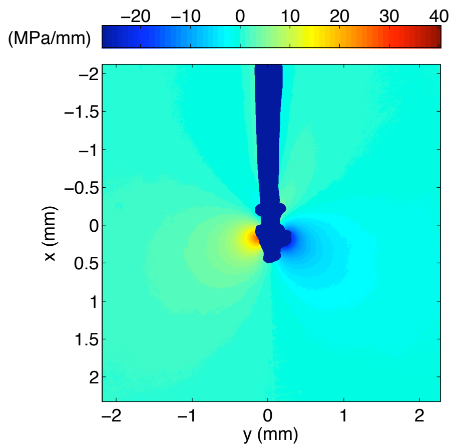

(c) Experimental $\frac{\partial(\sigma_1+\sigma_2)}{\partial y}$

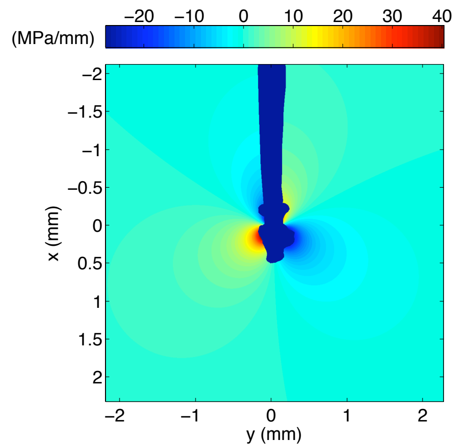

(d) Theoretical $\frac{\partial(\sigma_1+\sigma_2)}{\partial y}$

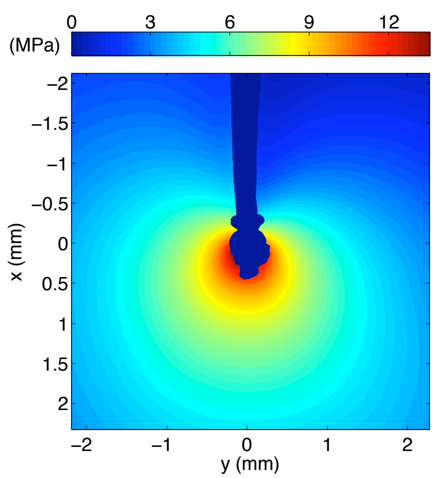

(e) Experimental $\sigma_1 + \sigma_2$

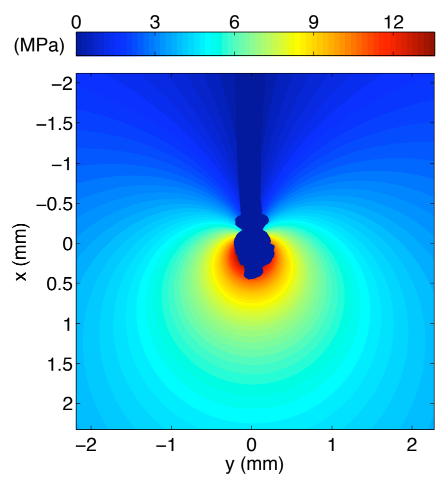

(f) Theoretical $\sigma_1 + \sigma_2$

Figure 4.61: Experimental and theoretical data for the derivatives of $\sigma_1 + \sigma_2$ and the experimental integrated $\sigma_1 + \sigma_2$ for specimen HomC2 for $K_I = 0.289$ MPa$\sqrt{\text{m}}$ and $K_{II} = -2.9$ kPa$\sqrt{\text{m}}$ with crack region masked in blue

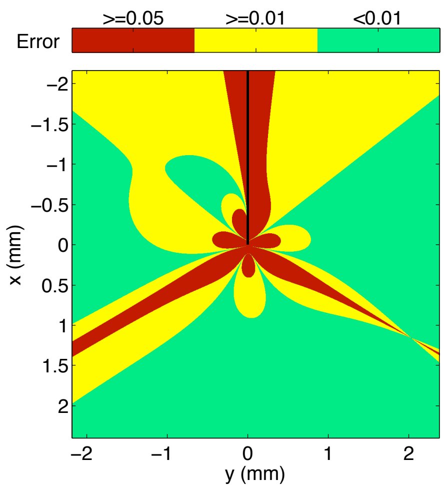

(a) Error for vertical shearing direction

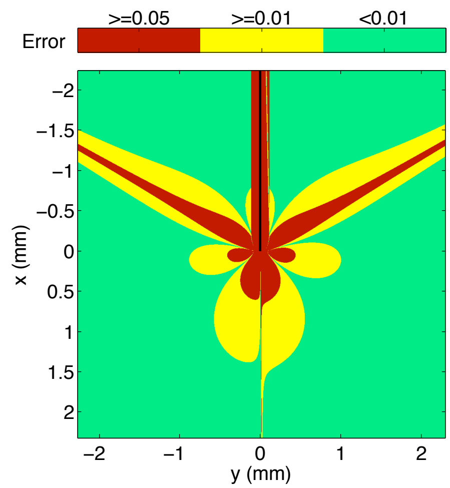

(b) Error for horizontal shearing direction

Figure 4.62: Theoretical error for CGS approximating the derivatives of $K_I = 0.289$ MPa$\sqrt{\text{m}}$ and $K_{II} = -2.9$ kPa$\sqrt{\text{m}}$ for the 4.6 mm $\times$ 4.6 mm field of view and lateral shearing distance of $d_{shear} = 225$ μm [Crack indicated in black]

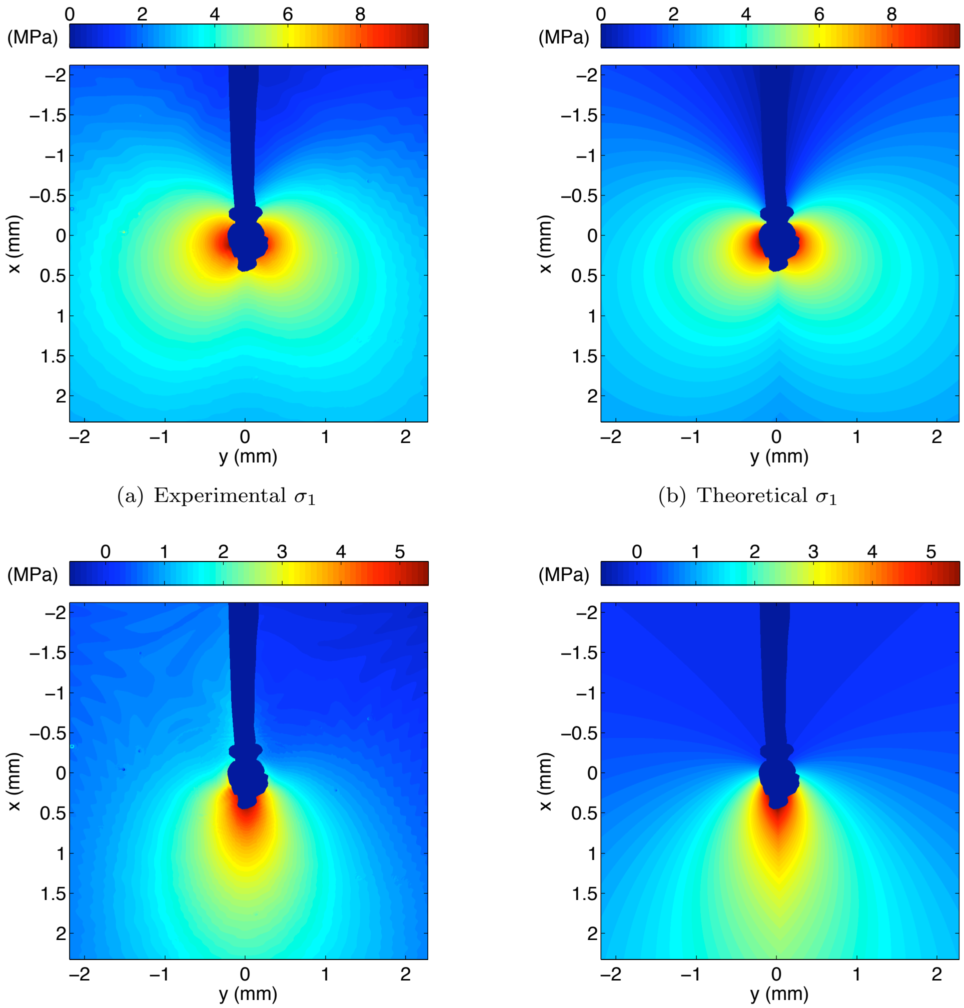

(a) Experimental σ_1

(b) Theoretical σ_1

(c) Experimental σ_2

(d) Theoretical σ_2

Figure 4.63: Experimental and theoretical data for the principal stresses for specimen HomC2 for $K_I = 0.289$ MPa$\sqrt{\text{m}}$ and $K_{II} = -2.9$ kPa$\sqrt{\text{m}}$ with crack region masked in blue

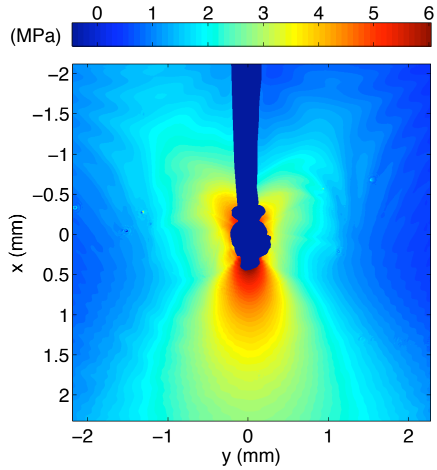

(a) Experimental σ_{xx}

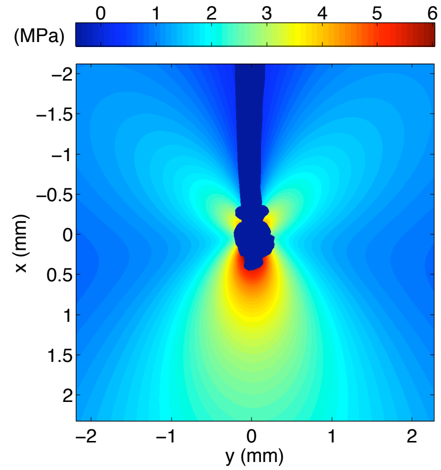

(b) Theoretical σ_{xx}

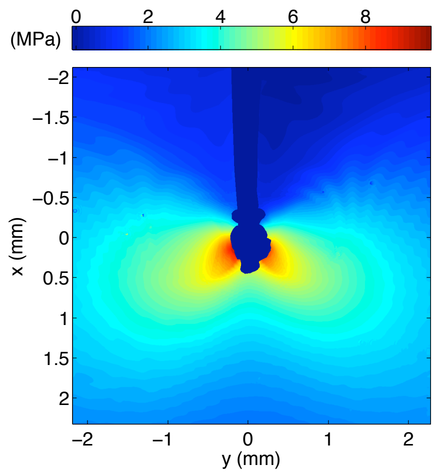

(c) Experimental σ_{yy}

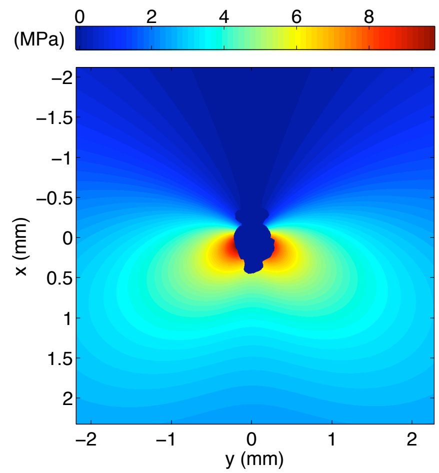

(d) Theoretical σ_{yy}

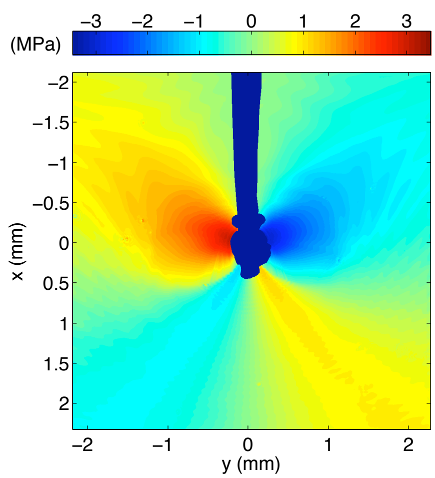

(e) Experimental σ_{xy}

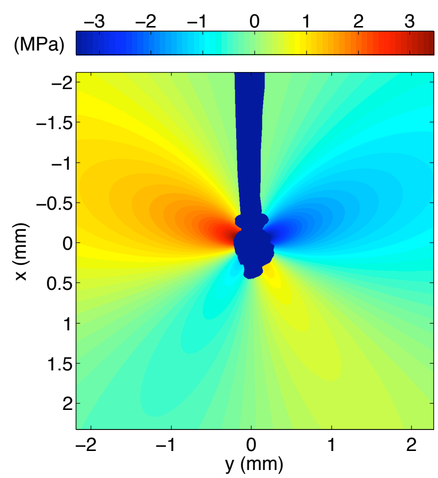

(f) Theoretical σ_{xy}

Figure 4.64: Experimental and theoretical data for the Cartesian stresses for specimen HomC2 for $K_I = 0.289$ MPa$\sqrt{\text{m}}$ and $K_{II} = -2.9$ kPa$\sqrt{\text{m}}$ with crack region masked in blue

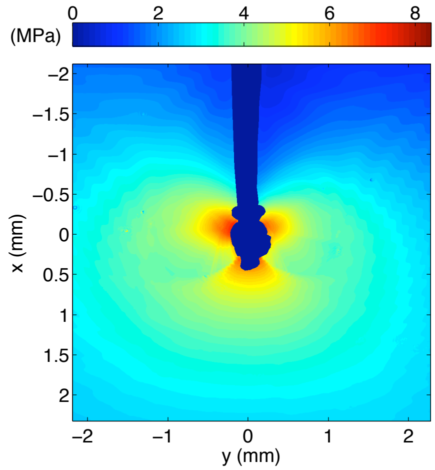

(a) Experimental σ_{rr}

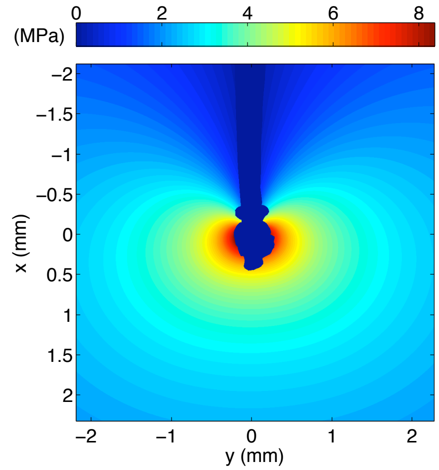

(b) Theoretical σ_{rr}

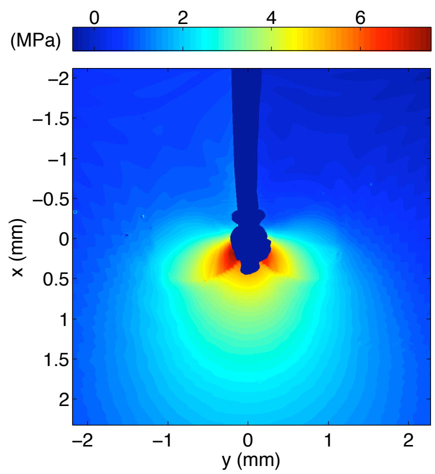

(c) Experimental $\sigma_{\theta\theta}$

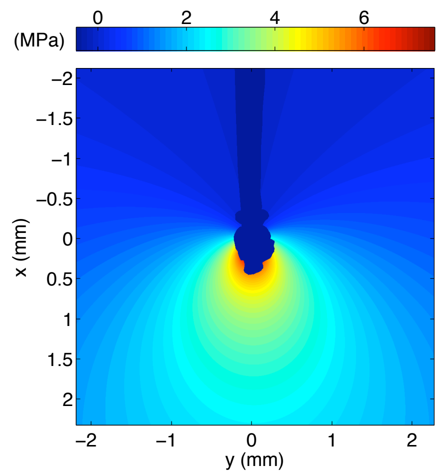

(d) Theoretical $\sigma_{\theta\theta}$

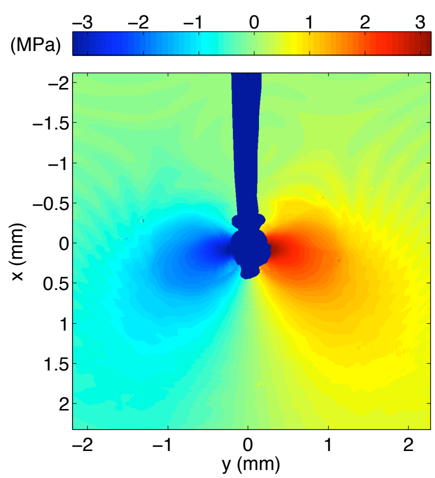

(e) Experimental $\sigma_{r\theta}$

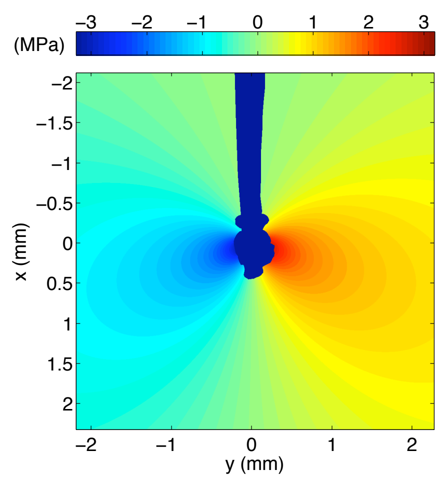

(f) Theoretical $\sigma_{r\theta}$

Figure 4.65: Experimental and theoretical data for the polar stresses for specimen HomC2 for $K_I = 0.289$ MPa$\sqrt{\text{m}}$ and $K_{II} = -2.9$ kPa$\sqrt{\text{m}}$ with crack region masked in blue

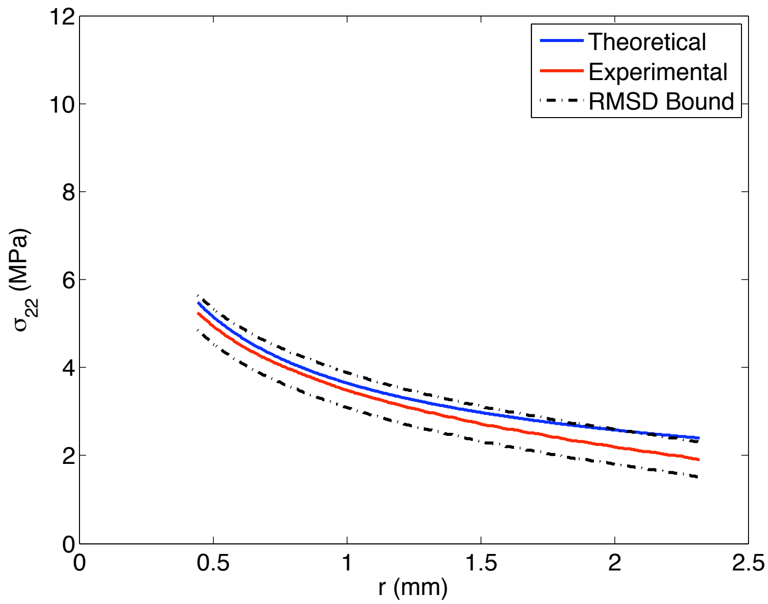

(a) σ_{yy} vs. r for $\theta = 0$

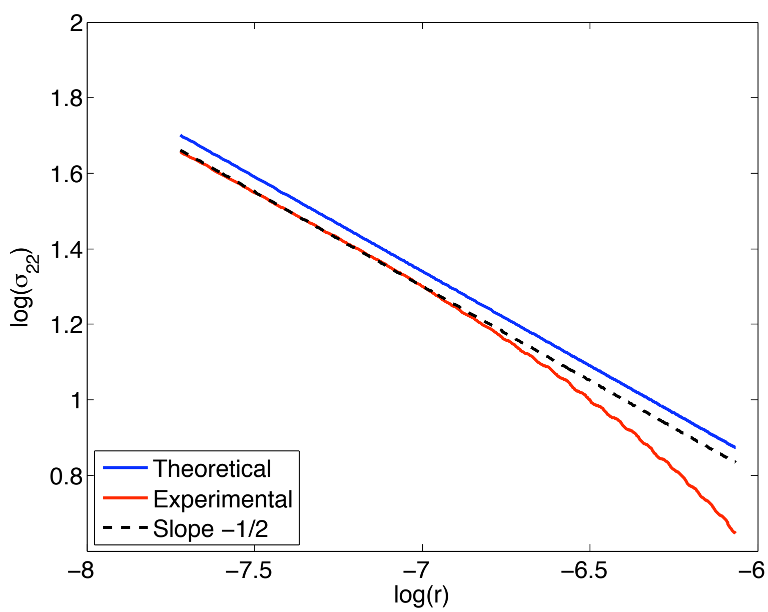

(b) $\log(\sigma_{yy})$ vs. $\log(r)$ for $\theta = 0$

Figure 4.66: Experimental and theoretical data for σ_{yy} along $\theta = 0$ for specimen HomC2 for $K_I = 0.289\ \mathrm{MPa}\sqrt{\mathrm{m}}$ and $K_{II} = -2.9\ \mathrm{kPa}\sqrt{\mathrm{m}}$: The experimental data is slightly lower than the theoretical data, but with similar $r^{-1/2}$ dependence seen by the near $-1/2$ slope on the log-log plot of σ_{yy} versus r.

4.3 Discussion of Experimental Method for Fracture Studies

The four Mode I–dominant, mixed-mode crack cases presented above demonstrate the ability of the hybrid experimental method to determine the in-plane tensorial stress around a crack in a photoelastic material. The full analysis of the highest K_I case establishes the validity of the experimental method to determine stress near a crack close to initial crack propagation, with the others demonstrating good quality data in a variety of cases. The different cases represent a significant range of K_I values for Homalite-100, whose fracture toughness is around 0.445 MPa$\sqrt{\text{m}}$ to 0.636 MPa$\sqrt{\text{m}}$ (Bradley and Kobayashi, 1971; Irwin et al., 1979; Dally, 1979): $K_I = 0.145$ MPa$\sqrt{\text{m}}$, $K_I = 0.259$ MPa$\sqrt{\text{m}}$, $K_I = 0.289$ MPa$\sqrt{\text{m}}$, and $K_I = 0.514$ MPa$\sqrt{\text{m}}$, which are from about $0.25K_{Ic}$ to $\sim K_{Ic}$. Each of these cases demonstrate K-dominant stress behavior, allowing for excellent comparison to the 2D asymptotic crack solution for a mixed-mode crack. This K dominance allows for calculation of the Mode I and Mode II stress intensity factors from a nonlinear least-squares fitting algorithm, excluding data points in the masked regions along the crack and a circle of radius $0.5h$ around the crack tip to remove points that may have 3D stress effects. Even though the K_I and K_{II} values come from full-field data from two different experimental techniques, these values lead to theoretical data that compare well with all of the experimental data, implying that CGS and photoelasticity are compatible for use in this hybrid method. If the K_I and K_{II} values only allowed for good agreement in a few fields, then the experimental method would be suspect. Across all of these cases, the NRMSD ranges from 0.012 to 0.078 with most of the fields below 0.05, indicating excellent global error for all of these cases. This experimental method also allows for determination of not only K_I values, but small K_{II} values as well, and therefore is able to detect small mode-mixity μ_{SIF} from -0.010 to 0.020. These small mode-mixities have a noticeable affect on the stress fields, giving rise to asymmetries in the stress fields that are apparent in the experimental data. Exclusion of K_{II} would lead to larger errors in the data by a few percent.

The four cases illuminate consistent error sources in the data. The rotational misalignment of the polarization optics, particularly the first $\lambda/4$ plate, lead to false discontinuities and zero-crossings that require manual correction. These corrections generally work, allowing for the determination of the isoclinic angle without detrimental and completely incorrect unwrapping. The isoclinic angle is a key component to the experimental method, so the manual corrections to the wrapped α field enable the method to work even with some localized errors in the subsequent stress fields. Obviously, a robust algorithm for correcting these errors due to polarization optic misalignment would improve confidence in the method, especially for fracture studies where the theoretical stress field solution is not known. In the cases presented in this chapter, the experimental isoclinic angle has error along the crack plane because the polarization optic misalignment leads to discontinuities near $\theta = 0$ that appear to be real discontinuities. Corrections here would not be simple and would require a variety of experiences with this method; hence, leaving the discontinuities as they are leads to α fields with known error sources, but with acceptable error levels. One way to reduce this need for corrections in the first place is to introduce strict polarization optic alignment techniques. Another error source in the data is the Fizeau fringes, but these are easily removed with anti-reflective coatings on the specimen.

The CGS assumption that the phase is related to a stress derivative is pushed to its limit due to three factors in this study: the small field of view, the finite shearing distance, and small mode-mixity. The first two factors work together to push the limit of the derivative assumption in that having a small field of view and requiring a reasonable phase sensitivity over a wide range of K_I cases requires a shearing distance that is a significant size relative to the field of view like the 5% of the side of the field of view in the cases presented above. Evident in the ϵ error analysis in Section 4.2.4.3, larger shearing distance produces more error in the derivative assumption over more area of the field of view. Also, the addition of a small K_{II} component appears to increase the ϵ error, particularly behind the crack for the shearing direction related to the x derivative, as the mode-mixity increases for the range of mode-mixity in this study. The effect of this on the stress fields is higher error behind the crack, seen with increasing severity with increasing mode-mixity. A full error analysis of the effect of mode-mixity on CGS derivative measurements is required if this method is applied to mixed-mode fracture cases. Characterization of these error sources explains the differences between experiment and theory in the cases presented here, but should not detract from the overall ability of this experimental method to determine full-field stresses around cracks in a photoelastic material. The experimental data have remarkable agreement with theory and allow for calculation of a range of stress intensity factors for Mode I–dominant cracks.

4.4 Conclusions

The hybrid CGS-photoelasticity experimental method is demonstrated for in-plane tensorial stress determination around Mode I–dominant cracks in Homalite-100 for a range of stress intensity factors for small fields of view, the first experimental study for full-field tensorial stress determination around cracks in photoelastic materials. Four cases across a range of $K_I = 0.145$ MPa$\sqrt{\text{m}}$ to $K_I = 0.514$ MPa$\sqrt{\text{m}}$, which is near the fracture toughness of Homalite-100, show K-dominant behavior, allowing for excellent comparison of the experimental stress fields with the 2D asymptotic crack solution for mixed-mode loading; the global error is less than 5% for most fields and no greater than 7.8%. The experimental method allows for calculation of K_I and small K_{II} values based on experimental data derived from both CGS and photoelasticity, showing that the two techniques work well together for stress determination. Common error sources over all four cases are characterized and can be mitigated with careful experimentation and with improved analysis algorithms. Overall, this experimental method successfully demonstrates the goal of stress determination near cracks in optically anisotropic, but otherwise isotropic materials, which lays the foundation for extending this method to studying stresses around cracks in anisotropic materials like crystals.